Heating and evaporation of a mono-component spheroidal droplet with non-uniform surface temperature

D.V. Antonov [a,b], S. Tonini [c], G.E. Cossali [c], P.A. Strizhak [a], S.S. Sazhin [b,d,*]

[a] *National Research Tomsk Polytechnic University, 30 Lenin Avenue, Tomsk, 634050, Russian Federation*

[b] *Kutateladze Institute of Thermophysics Siberian Branc, Russian Academy of Sciences, 1 Lavrentiev Avenue, Novosibirsk 630090, Russian Federation*

[c] *Department of Engineering and Applied Sciences, Università degli Studi di Bergamo, Viale Marconi 6, 24044 Dalmine (BG), Italy*

[d] *Advanced Engineering Centre, School of Architecture, Technology and Engineering, University of Brighton, Brighton, BN2 4GJ, United Kingdom*

ARTICLE INFO

ABSTRACT

A new mathematical model for spheroidal droplet heating and evaporation is proposed. This model takes into account the effect of liquid finite thermal conductivity and is based on the previously obtained analytical solution for the vapour mass fraction at the droplet surface and a new correlation for the convective heat transfer coefficient incorporated into the numerical code. The heat transfer equation in the liquid phase is solved numerically using the finite-element heat transfer module of COMSOL Multiphysics. It is shown that the lifetime of spheroidal (prolate and oblate) droplets is shorter than that of spherical droplets of the same volume. The difference in the lifetimes of spheroidal and spherical droplets, predicted by the new model, is shown to increase with increasing aspect ratios for prolate droplets and decreasing aspect ratios for oblate droplets. As in the case of stationary spherical droplets, the d^2-law is shown to be valid for spheroidal droplets after the completion of the heat-up period. The predictions of this model agree with experimental observations. The duration of the heat-up period is shown to decrease with increasing aspect ratios for prolate droplets and decreasing aspect ratios for oblate droplets. The maximal surface temperatures are predicted near the regions where the surface curvature is maximal. The aspect ratios are shown to be weak functions of time, in agreement with experimental observations.

1. Introduction

The majority of the models of droplet evaporation and heating developed so far have assumed that droplets are spherical although in many industrial applications this assumption is not valid [1]. Non-spherical droplets are commonly observed in internal combustion engine sprays [2,3]. It is not feasible to develop a model for evaporation and heating of droplets of arbitrary shapes except by using direct numerical simulations [4,5], the application of which for practical engineering problems is limited. They cannot be incorporated in in-house or commercial CFD (Computational Fluid Dynamics) codes [6]. Also, these simulations of a complex process such as droplet evaporation do not always help to understand the physics of the individual processes, since overlapping of many

Nomenclature

English symbols

a	parameter defined by Expression (3)	m
A	area	m^2
$a_r(a_z)$	radial (axial) droplet semi-axes	m
B_M	Spalding mass transfer number	-
c	specific heat capacity	J/(kg K)
D	diffusion coefficient	m^2/s
f_1	function defined by Expression (22)	-
G	$\ln(1 - Y_v)$	-
g_n	parameter defined by Expression (5)	-
h	local convective heat transfer coefficient (non-uniform surface temperature)	W/(m^2 K)
h_u	convective heat transfer coefficient (uniform surface temperature)	W/(m^2 K)
k	thermal conductivity	W/(m K)
Le	Lewis number	-
M	molar mass	kg/kmole
m_d	droplet mass	kg
$\dot{m}_d$	droplet evaporation rate	kg/s
m_e''	mass evaporation flux	kg/(m^2 s)
P	pressure	Pa
q_{ev}	heat flux due to evaporation	W/m^2
$\dot{q}$	heat flux	W/m^2
r	spherical coordinate	m
R_0	effective radius	m
R_d	droplet radius	m
t	time	s
T	temperature	K
t_d	characteristic time of diffusion	s
t_e	characteristic time of evaporation	s
t_o	characteristic time of oscillation	s
v	velocity of the recession of a surface	m/s
W_0^α	function defined by Expression (6)	-

W_n^α	function defined by Expression (7)	-
x, y, z	Cartesian coordinates	m
Y_v	mass fraction of vapour	-

Greek symbols

α	$\alpha = 1$ (prolate) or $\alpha = 2$ (oblate)	-
β, γ	parameters defined by Expressions (29) and (30)	-
ε	aspect ratio	-
ζ, η, ϕ	elliptical coordinates	m
θ	spherical coordinate	m
ρ	density	kg/m^3
σ	surface tension	kg/s^2

Subscripts

a	air
cor	correlation
d	droplet
ev	evaporation
eff	effective
f	fuel
g	gas
l	liquid
max	maximum
n	normal component
num	numerical
r	radial component
s	surface
T	total
sat	saturated
v	vapour
z	axial component
0	initial state
∞	ambient condition

phenomena in most cases hides the importance of each single one. The importance of each phenomenon can be better understood when the others are switched off, as is the case in relatively simple models like the one that is the focus of this paper. In most simple models of this kind, it has been assumed that non-sphericity of droplets can be approximated by oblate or prolate spheroids.

Niven [7] was the first (to the best of our knowledge) to solve analytically the heat transfer equation in a spheroid, 143 years ago. Complementary analytical solutions to this equation for steady state temperature distribution near a prolate spheroid were presented in [8].

These approaches, however, were focused on the problem of the heating of spheroidal bodies and their direct application to the investigation of droplet evaporation and heating is limited. Grow [9] seems to have been the first to solve the problem of mass and heat transfer near spheroidal particles, using the assumption of their zero relative velocities. The key limitation of her analysis is that both heat and mass transfer equations were presented as Laplace equations, which are valid only when the effects of the Stefan flow from the particle surfaces are not considered. The effects of this flow were described using the analytical solutions to the heat and mass transfer equations in the gas phase near a spheroidal droplet by Tonini and Cossali [10]. The key assumption of their analysis was that there is no temperature gradient along the droplet surface. They assumed that evaporation does not affect the droplet's spheroidal shape.

A problem of spheroidal droplet evaporation and heating, as in [10], was considered in [11]. Li and Zhang [11] focused on the gas phase species conservation equation. Similarly to [10], they used the assumption of infinitely large liquid thermal conductivity. Contrary to [10], in [11] the relative velocities of droplets were taken into account, assuming that the dependencies of the Sherwood and Nusselt numbers on the Schmidt, Prandtl and Reynolds numbers are not affected by droplet eccentricities. Li and Zhang [11] considered the dependencies of droplet temperatures and sizes on time, focusing on oblate droplets.

Zubkov et al. [12] generalised the model developed in [10] to consider the contribution of finite liquid thermal conductivity. Their analysis used a combination of the analytical gas phase model described in [10] and the numerical analysis of the heat transfer process in the liquid. We call this model semi-analytical. The model presented in [12] assumed that the droplets are close to spherical. The temperature gradient in the direction along the droplet surface was assumed to be small compared to that in the direction normal

to this surface. These assumptions limit the applicability of this model to practical engineering applications and are relaxed in the new model, the results of the development of which are presented in Section 2.

The new model described in the current paper uses the gas phase model described by Tonini and Cossali [13] and the numerical solution to the heat conduction equation in the liquid phase using the boundary conditions inferred from the model presented in [13]. Thus, we refer to the new model as semi-analytical as in the case of the model presented in [12]. In contrast to [13], no restrictions are imposed on the values of the liquid thermal conductivity. In contrast to Ref. [12], no restrictions are imposed on the eccentricity of the spheroid and the gradients of vapour mass fractions and temperature along the surface of the spheroid. Thus, we can consider the new model to be a generalisation of the previously developed semi-analytical models of spheroidal droplet evaporation and heating. The lack of restrictions imposed in the previously described models makes the new model particularly attractive for practical engineering applications.

We need to emphasise that no attempts to generalise the analytical solution obtained in [7] have been made since the publication of [7], to the best of our knowledge. The solution obtained in [7] cannot be used in our analysis as this solution is based on uniform Dirichlet boundary conditions and does not consider the effects of non-uniformity of droplet surface temperature on which the present paper is focused.

The details of the new model are described in Section 2. Section 3 focuses on the solution procedure. The predictions of the new model are verified in Section 4. In Section 5 the predictions of the new model for a wide range of input parameters are investigated. The validation of the new model is discussed in Section 6. The key findings of the paper are summarised in Section 7.

2. Mathematical model

The mathematical model used in our analysis is based on the modified and extended version of the gas phase model of mass/heat transfer from/to spheroidal droplets described in [13]. The predictions of the gas phase model, described in Section 2.1 will be used as the boundary conditions for the liquid phase model described in Section 2.2.

2.1. Gas phase model

The model described in [13] is based on the assumption that all processes are quasi-steady-state and all transport and thermo-dynamic properties are constant during each timestep (they can change from one timestep to another). The problem was solved in spheroidal coordinates defined as [14]:

$$x = a\sqrt{\zeta^2 - 1}\sqrt{1 - \eta^2}\cos\varphi; \quad y = a\sqrt{\zeta^2 - 1}\sqrt{1 - \eta^2}\sin\varphi;$$

$$z = a\zeta\eta \quad \text{(prolate)} \tag{1}$$

$$x = a\sqrt{\zeta^2 + 1}\sqrt{1 - \eta^2}\cos\varphi; \quad y = a\sqrt{\zeta^2 + 1}\sqrt{1 - \eta^2}\sin\varphi;$$

$$z = a\zeta\eta \quad \text{(oblate)}. \tag{2}$$

The coordinate space is limited as

$$1 \leq \zeta < \infty; \quad -1 \leq \eta \leq 1; \quad 0 \leq \varphi \leq 2\pi$$

for prolate spheroids and

$$0 \leq \zeta < \infty; \quad -1 \leq \eta \leq 1; \quad 0 \leq \varphi \leq 2\pi$$

for oblate spheroids.

A schematic presentation of spheroidal coordinate systems for prolate and oblate spheroids is shown in Fig. 1.

The surfaces $\zeta = \text{const}$ are prolate spheroids (for the prolate spheroidal system) or oblate spheroids (for the oblate spheroidal system); the surfaces $\eta = \text{const}$ are hyperboloids and the surfaces $\varphi = \text{const}$ are half planes passing by the z-axis. In both cases the droplet surface can be fitted into an iso-coordinate surface by defining it as $\zeta = \zeta_0$.

Formulae (1) and (2) reduce to the spherical coordinate system when $\eta = \cos\theta$ and $\zeta = \sqrt{r^2 + 1}$ (prolate) or $\zeta = \sqrt{r^2 - 1}$ (oblate), where $r = \sqrt{x^2 + y^2} \geq 1$.

Introducing R_0 as the radius of a sphere which has the same volume as the spheroid (effective radius), parameter a can be estimated as:

$$a = R_0 \frac{\left|1 - \varepsilon^2\right|^{1/2}}{\varepsilon^{1/3}}, \tag{3}$$

where $\varepsilon = \frac{a_z}{a_r}$ (aspect ratio), a_r and a_z are radial and axial droplet semi-axes.

The analytical solution to the vapour mass conservation equation in these coordinate systems was presented as [13]:

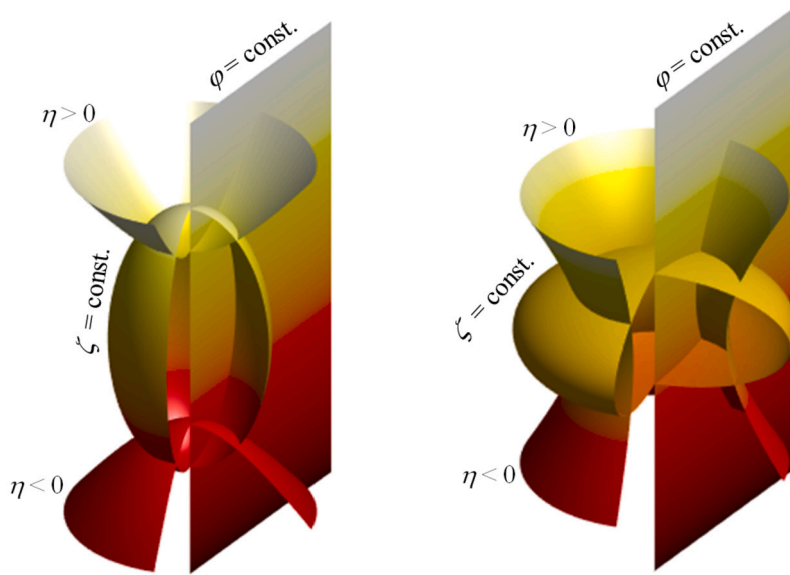$$G = g_0 W_0^\alpha(\zeta) + \sum_{n=1}^\infty g_n P_n(\eta) W_n^\alpha(\zeta) + G_\infty \tag{4}$$

Fig. 1. A schematic presentation of spheroidal coordinate systems for prolate (left) and oblate (right) spheroids.

where

$$g_n = \int_{-1}^{1} G_s^\alpha (\eta) P_n (\eta) \, d\eta \tag{5}$$

$$W_0^\alpha (\zeta) = \begin{cases} \dfrac{1}{2} \dfrac{\ln \frac{\zeta-1}{\zeta+1}}{\ln \frac{\zeta_0-1}{\zeta_0+1}} & \alpha = 1; \text{ prolate} \\ \dfrac{1}{2} \dfrac{\arctan(\zeta)-\pi/2}{\arctan(\zeta_0)-\pi/2} & \alpha = 2; \text{ oblate} \end{cases} \tag{6}$$

$$W_n^\alpha (\zeta) = \begin{cases} \dfrac{2n+1}{2} \dfrac{Q_n(\zeta)}{Q_n(\zeta_0)} & \alpha = 1; \text{ prolate} \\ \dfrac{2n+1}{2} \dfrac{Q_n(i\zeta)}{Q_n(i\zeta_0)} & \alpha = 2; \text{ oblate,} \end{cases} \tag{7}$$

$$G = \ln(1 - Y_v) \tag{8}$$

(Y_v is the mass fraction of vapour), P_n are the Legendre polynomials, and Q_n are the Legendre functions of the second kind of integer degree and zero order. P_n and Q_n can be calculated as [14]:

$$P_n(x) = \frac{1}{2^n n!} \frac{\mathrm{d}^n \left[\left(x^2 - 1\right)^n \right]}{\mathrm{d}x^n}, \tag{9}$$

$$Q_n(x) = \frac{1}{2} P_n \ln \left(\frac{1+x}{1-x} \right) - \sum_{k=1}^{k=n} \frac{P_{k-1}(x) P_{n-k}(x)}{k} \quad (n > 0). \tag{10}$$

The conditions at the droplet surface and at infinity

$$G \left(\zeta = \zeta_0, \eta \right) = G_s (\eta); \quad G (\zeta = \infty, \eta) = G_\infty \tag{11}$$

allowed Tonini and Cossali [13] to obtain the coefficients g_n and the constant G_∞. The value of G at infinity was assumed to be constant since the vapour mass fraction is considered uniformly distributed at an infinite distance from the droplet. Note that

$$G_s (\eta) = \ln \left(1 - \frac{P_{v,sat} \left(T_s (\eta) \right) M_v}{P_{v,sat} \left(T_s (\eta) \right) \left(M_v - M_a \right) + P_T M_a} \right), \tag{12}$$

where M_v and M_a are molar masses of vapour and air, P_T is the total pressure of the mixture of air and vapour.

Following [13], six terms in the series in (4) were used in our analysis as a compromise between an acceptable accuracy in reproducing the surface distribution of the function G and relatively low computational costs.

The components of the mass fluxes are estimated as:

$$\dot{m}''_{d\,(\zeta)} = \rho D_{10} \frac{1}{\sqrt{g_{\zeta\zeta}}} \frac{\partial G}{\partial \zeta} = \rho D_{10} \frac{1}{\sqrt{g_{\zeta\zeta}}} \left[g_0 W_0'^\alpha (\zeta) + \sum_{n=1}^{\infty} g_n P_n (\eta) W_n'^\alpha (\zeta) \right] \tag{13}$$

$$\dot{m}''_{d\,(\eta)} = \rho D_{10} \frac{1}{\sqrt{g_{\eta\eta}}} \frac{\partial G}{\partial \eta} = \rho D_{10} \frac{1}{\sqrt{g_{\eta\eta}}} \left[\sum_{n=1}^{\infty} g_n P'_n(\eta) W_n^\alpha(\zeta) \right], \tag{14}$$

where

$$g_{\eta\eta} = a^2 \left(\frac{\zeta^2 - \eta^2}{1 - \eta^2} \right); \quad g_{\zeta\zeta} = a^2 \left(\frac{\zeta^2 - \eta^2}{\zeta^2 - 1} \right); \quad \text{prolate}$$

$$g_{\eta\eta} = a^2 \left(\frac{\zeta^2 + \eta^2}{1 - \eta^2} \right); \quad g_{\zeta\zeta} = a^2 \left(\frac{\zeta^2 + \eta^2}{\zeta^2 + 1} \right); \quad \text{oblate}$$

$W'^\alpha_n(\zeta)$ and $P'_n(\eta)$ are the derivatives of $W_n^\alpha(\zeta)$ and $P_n(\eta)$ with respect to their independent variable.

Note that at the surface of the droplet $\zeta = \zeta_0$ only the component $\dot{m}''_{d\,(\zeta)}$ (mass flux normal to the droplet surface) contributes to the evaporation process.

Unfortunately, Tonini and Cossali [13] were not able to obtain analytical expressions similar to (13) and (14) for heat fluxes. In what follows, approximate expressions for these fluxes, to be used in our analysis, are obtained.

If the surface temperature is uniform, then the heat transfer coefficient, h_u can be calculated analytically [13]:

$$\begin{aligned} h_u(\eta) &= \frac{2k}{h_\zeta(\eta)} \left(\frac{e^{-Z}}{1 - e^{-Z}} Z \right) \left(\frac{dW_0^\alpha}{d\zeta} \right)_{\zeta = \zeta_0} \\ Z &= \frac{1}{Le} \ln \left(\frac{1 - Y_\infty}{1 - Y_s} \right), \end{aligned} \tag{15}$$

where Le is the gas Lewis number, W_0^α is defined by Expression (6).

Expression (15) is identical to Expression (14) of [12].

This expression allows us to estimate the heat flux reaching an element of the droplet as

$$\dot{q} = h(T_g - T_s), \tag{16}$$

where T_g and T_s are ambient gas and droplet surface temperatures, respectively; h is the local convective heat transfer coefficient for non-uniform temperature distribution at the droplet surface.

Our approach to estimation of the local values of h in the case of non-uniform surface temperature is based on the approximation of the results of numerical estimation of this parameter, presented in [13]. Tonini and Cossali [13] introduced the parameter

$$\Delta = \frac{\hat{h} - \hat{h}_u}{\hat{h}_u}, \tag{17}$$

where $\hat{h} = 2h R_{d0}/k_g$, $\hat{h}_u = 2h_u R_{d0}/k_g$, R_{d0} is the initial droplet equivalent radius (radius of a sphere with a volume equal to that of a spheroid), k_g is the thermal conductivity of a mixture of air and vapour.

Δ for a given species (n-dodecane) depends on η, ε, $\bar{T}_s$ (the average surface temperature), and T_g (see Figures 6, 8, 10 and 11 of [13]). As follows from Figure 9 of Ref. [13], Δ is proportional to $\Delta T_{\max}$ (the maximal variation of the temperature on the droplet surface). Thus we can write:

$$\Delta = g\left(\eta, \varepsilon, \bar{T}_s, T_\infty\right) \Delta T_{\max} \tag{18}$$

or

$$\frac{\hat{h}}{\hat{h}_u} = 1 + g\left(\eta, \varepsilon, \bar{T}_s, T_\infty\right) \Delta T_{\max}. \tag{19}$$

In [13] the temperature distribution was chosen to satisfy the conditions

$$|T(\eta = 1) - T(\eta = 0)| = \Delta T_{\max} \tag{20}$$

$$\left(\frac{\partial T}{\partial \eta} \right)_{\eta = 1} = 0; \quad \frac{T(\eta = 1) + T(\eta = 0)}{2} = \bar{T}_s. \tag{21}$$

Let us introduce the new function

$$f_1(\eta) = \frac{T - \bar{T}_s}{\Delta T_{\max}}. \tag{22}$$

We look for the following approximation of $f_1(\eta)$:

$$f_1(\eta) = a\eta^4 + b\eta^2 + c. \tag{23}$$

Only even powers of η were used in (23) to satisfy the symmetry condition at the droplet equator ($\eta = 0$).

It follows from Equations (20) and (21) that $a = 2c$, $b = -2a$ and $c = \frac{\text{sign}(T_0 - T_1)}{2}$, where $T_0 = T(\eta = 0)$ and $T_1 = T(\eta = 1)$.

The dependence of $g\left(\eta, \varepsilon, \bar{T}_s, T_\infty\right)$ on η is presented as

$$g\left(\eta, \varepsilon, \bar{T}_s, T_\infty\right) = \alpha^{(1)}\left(\varepsilon, \bar{T}_s, T_\infty\right) f_1(\eta). \tag{24}$$

This leads to the following presentation of $\frac{\hat{h}}{\hat{h}_u}$:

$$\frac{\hat{h}}{\hat{h}_u} = 1 + \alpha^{(1)}\left(\varepsilon, \bar{T}_s, T_\infty\right) f_1(\eta)\Delta T_{\max}$$
$$= 1 + \alpha^{(1)}\left(\varepsilon, \bar{T}_s, T_\infty\right)\left(T(\eta) - \bar{T}_s\right). \tag{25}$$

The following procedure is suggested for finding $\alpha^{(1)}\left(\varepsilon, \bar{T}_s, T_\infty\right)$ in Correlation (25). Considering the case shown in Figure 8a of [13] ($\bar{T}_s = 380K$ and $T_\infty = 700K$), we can use the power law interpolation of the curves shown in this figure:

$$\Delta_{\max}(\varepsilon, 380, 700) = \beta \Delta T_{\max}\varepsilon^{-\gamma}. \tag{26}$$

Remembering that $|f_1| \le 0.5$, Equations (18) and (24) allow us to write

$$\frac{\Delta_{\max}}{\Delta T_{\max}} = g\left(\eta_0, \varepsilon, \bar{T}_s, T_\infty\right) = \frac{1}{2}\alpha^{(1)}\left(\varepsilon, \bar{T}_s, T_\infty\right). \tag{27}$$

From (26) and (27) it follows that

$$\alpha^{(1)}\left(\varepsilon, \bar{T}_s, T_\infty\right) = \beta\left(\bar{T}_s, T_\infty\right)\varepsilon^{-\gamma\left(\bar{T}_s, T_\infty\right)}. \tag{28}$$

Functions $\beta\left(\bar{T}_s, T_\infty\right)$ and $\gamma\left(\bar{T}_s, T_\infty\right)$ are found by interpolating the data shown in Figures 10 and 11 of [13]:

$$\gamma\left(\bar{T}_s, T_\infty\right) = 0.849 - 1.5 \times 10^{-4}T_\infty - 1.4 \times 10^{-3}\bar{T}_s \tag{29}$$

$$\beta\left(\bar{T}_s, T_\infty\right) = -0.0377 - 1.62 \times 10^{-5}T_\infty + 1.64 \times 10^{-4}\bar{T}_s, \tag{30}$$

where all temperatures are in K.

This leads to the final correlation

$$\frac{\hat{h}}{\hat{h}_u} = 1 + \beta\left(\bar{T}_s, T_\infty\right)\varepsilon^{-\gamma\left(\bar{T}_s, T_\infty\right)}\left(T(\eta) - \bar{T}_s\right). \tag{31}$$

Correlation (31) is used to find the local heat transfer coefficient $\hat{h}$ as a function of $\hat{h}_u$. This correlation shows an explicit dependence of the heat transfer coefficient on the local surface temperature, inferred from the numerical results presented in [13]. The results presented in [13] for n-dodecane prolate and oblate droplets evaporating in air at various operating conditions are used to obtain the coefficients in Eqs. (29) and (30). Fig. 2 shows a comparison between the numerical results $\left(\frac{\hat{h}}{\hat{h}_u}\right)_{num}$ and the values predicted by Correlation (31) $\left(\left(\frac{\hat{h}}{\hat{h}_u}\right)_{cor}\right)$ for prolate and oblate droplets. The maximal discrepancy between the numerical data presented in [13] and the predictions using Correlation (31) was found to be 4.2%. Note that different conditions for which numerical data were obtained may yield different coefficients in Equations (29) and (30). Also, different correlation selections may yield different levels of agreement with numerical data. We need to emphasise that the aim of the present investigation is to show the applicability of the new approach to the analysis of the effect of non-uniform surface temperature, rather than to demonstrate the validity of the proposed correlation.

2.2. Liquid phase model

The analytical solution to the vapour mass transfer equation and the correlation for the heat transfer in the gas phase around a spheroidal droplet, described in Section 2.1, were used as boundary conditions for the heat transfer equation in the liquid phase. The temperature gradients inside the droplet and at its surface, and the changes in their shape during the heating and evaporation process, were considered, although the droplet was assumed to remain spheroidal. As in [12] the effects of droplet motion and surface tension on droplet heating and evaporation were not considered. In contrast to [12] no specific restrictions on the eccentricity of the spheroid were imposed in our analysis apart from the assumption that Correlation (31) is valid.

The following transient heat transfer equation in the liquid phase was solved numerically [12]:

$$\rho_l c_l \frac{\partial T}{\partial t} - \nabla(k_l \nabla T) = 0, \tag{32}$$

where ρ_l, k_l, and c_l are liquid density, thermal conductivity, and specific heat capacity, respectively.

Equation (32) was solved subject to the boundary condition

$$-\mathbf{n}(-k_l \nabla T) = q_{\mathrm{ev}} + h(T_g - T_s) \qquad \text{at} \qquad \zeta = \zeta_0, \tag{33}$$

where $\mathbf{n}$ is the unit vector normal to the droplet surface, q_{ev} is the latent heat of evaporation [6]. The convective heat transfer coefficient h predicted by Correlation (31) was used.

The droplet evaporation was considered but not its thermal swelling. The droplet shape was recalculated at the end of each time step assuming that the droplet remains spheroidal. For the case of isothermal droplets without internal flows or external forces this was rigorously proven in [12]. In that case, the uniform Dirichlet boundary conditions yield a mono-dimensional solution to the species and energy conservation equations in spheroidal coordinates. The latter also ensured the constancy of the droplet aspect
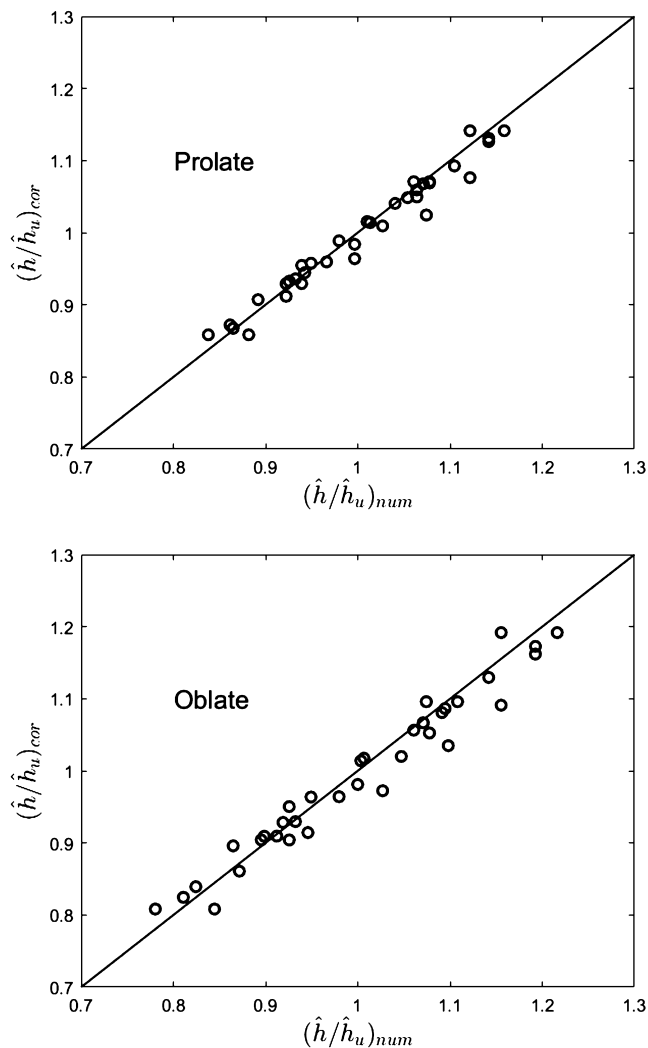
Fig. 2. Comparison between the numerical results $\left(\left(\frac{\hat{h}}{\hat{h}_u}\right)_{num}\right)$ and the values given by Correlation (31) $\left(\left(\frac{\hat{h}}{\hat{h}_u}\right)_{cor}\right)$ for prolate (top) and oblate (bottom) droplets.

ratio. The changes in the size of the droplet perpendicular to and along the z-axis over time follow from the following expressions [12]:

$$a'_r(t) = -\frac{1}{\rho_l}\left.\frac{\mathrm{d}\dot{m}_{d\,\mathrm{ev}}}{\mathrm{d}A}\right|_{u=\pi/2}, \qquad a'_z(t) = -\frac{1}{\rho_l}\left.\frac{\mathrm{d}\dot{m}_{d\,\mathrm{ev}}}{\mathrm{d}A}\right|_{u=0}, \tag{34}$$

where $\frac{\mathrm{d}\dot{m}_d}{\mathrm{d}A}$ is the evaporation mass flux.

The following initial conditions were used

$$a_r(0) = a_{r0}, \qquad a_z(0) = a_{z0}. \tag{35}$$

The vapour density and temperature at the droplet surface were linked by the ideal gas law. $\rho_{v\infty}$ was assumed equal to zero.

The normal component of velocity of the surface of the evaporating droplet v_n was estimated as [12]:

$$v_n = v_r n_r + v_z n_z, \tag{36}$$

$$v_r = r(r^2 a'_r/a_r^3 + z^2 a'_z/a_z^3), \qquad v_z = z(r^2 a'_r/a_r^3 + z^2 a'_z/a_z^3), \tag{37}$$

$$n_r = r/a_r^2\sqrt{r^2/a_r^4 + z^2/a_z^4}, \qquad n_z = z/a_z^2\sqrt{r^2/a_r^4 + z^2/a_z^4}. \tag{38}$$
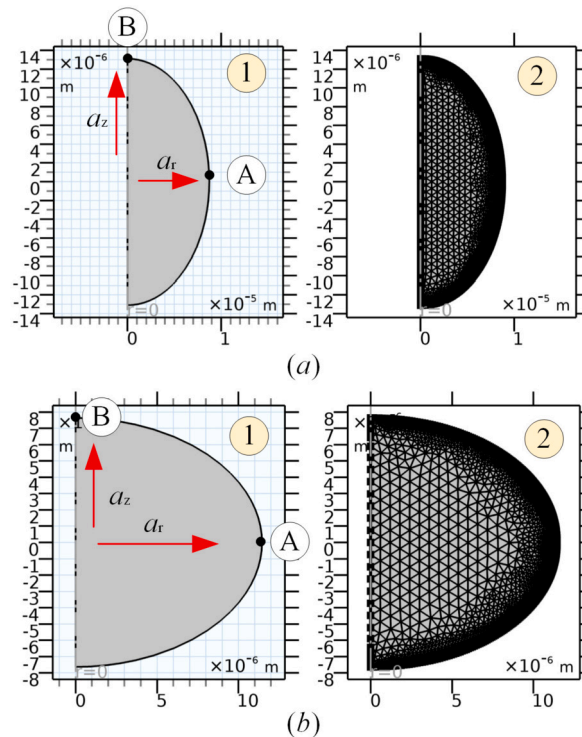
Note typos in Expressions (29)-(30) of [12].

Fig. 3. The geometry (1) and mesh (2) used for numerical simulations: (a) – prolate ($\varepsilon = 1.5$) and (b) – oblate ($\varepsilon = 2/3$) spheroids. The model is axisymmetric around the vertical axis (the dotted-dashed line). Mesh parameters: maximum element size 7.4×10^{-7} m, minimum element size 2.5×10^{-9} m, maximum element growth rate 1.25, curvature factor 0.01. Fine mesh was used near the droplet surfaces.

The contribution of natural convection and the Marangoni effect (see [15] and the references in this paper) are not considered. The temperature dependence of all transport and thermodynamic properties was considered in numerical simulations using our new model.

The key assumptions of the model described in our paper are similar to those used in [17–19] which considered a different problem of droplet evaporation on a substrate. The key difference in our approaches is that the authors of [17–19] based their investigation on purely numerical analysis of the conservation equations, while a combined analytical/numerical analysis is used in this paper.

3. Solution procedure

Equations (32)-(34) were solved numerically using the finite-element heat transfer module of COMSOL Multiphysics. It was assumed that the droplet remains axisymmetric. Approximations of key thermodynamic and transport properties of air, liquid and vapour n-dodecane are presented in Table 1. All droplet properties were recalculated at the ends of the time steps for updated average droplet temperatures.

The computational geometry and mesh domains are shown in Fig. 3a for prolate ($\varepsilon = 1.5$) and Fig. 3b for oblate ($\varepsilon = 2/3$) spheroids. A deformed geometry with mesh smoothing type Yeoh was used. The stiffening factor was 10, and a prescribed normal mesh velocity type was used to describe the moving interface due to evaporation effects. As a result, the droplet surface was allowed to move to optimise the droplet shapes. Automatic remeshing was used to control mesh quality at deformed geometry.

It was ensured that the solutions remained unaffected by the mesh size and time steps below certain minimal values were used. The minimum element quality, element area ratio, and grid element convergence index (GCI) were evaluated for four grids with initial numbers of cells ranging from 554 to 27,491. The calculation of the GCI was based on the procedure for estimation of uncertainty due to discretisation described in [20]. The grid with initial number of cells equal to 4528 was used for calculations.

The calculations were performed on a quad-core PC (3.4 GHz Intel Core i5-3570 CPU, 32 GB, 64K L1 cache, 1 MB L2 cache). Typical computation times were in the range 5 to 100 minutes. For example, the computational time for the case of an n-dodecane droplet with $R_{d0} = 10$ μm, $\varepsilon = 1.5$, $P_g = 30$ bar, $T_g = 700$ K, $T_0 = 300$ K was 34 minutes.
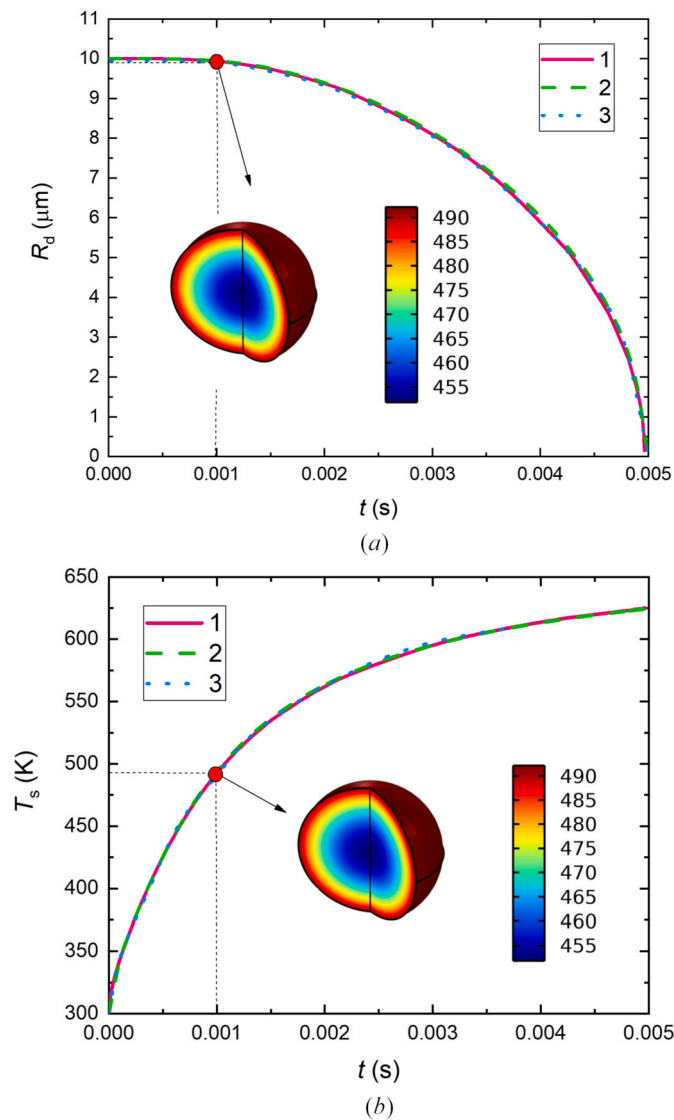
Fig. 4. Plots of spherical droplet radii R_d (a) and surface temperatures T_s (b) versus time predicted by the model described in this paper (1), in-house MATLAB code (2) and the model developed by Zubkov et al. [12] (3) for the input parameters described in Section 4.

4. Verification of the results

To verify the results of calculations we considered an n-dodecane droplet with initial radius 10 μm and initial temperature 300 K placed in air at temperature 700 K and pressure 30 bar. Note that Correlation (31) was obtained for atmospheric pressure. It was not, however, used in the verification procedure, in which the droplet was assumed to be spherical. Thermodynamic and transport properties of liquid and vapour n-dodecane and air are presented in Appendix A.

Verification of the results was based on a comparison between the predictions of the code in the limiting case of a spherical droplet, the predictions of the MATLAB code specifically developed for spherical droplets, and the predictions of the code for spheroidal droplets (close to spherical droplets), developed by Zubkov et al. [12] in the limiting case of spherical droplets. The results of the comparison between the predictions of these three codes are presented in Fig. 4. As can be seen in this figure, the predictions of all three codes almost coincide within the accuracy of plotting. The differences between the results are less than about 1%. These differences are comparable with the expected errors in calculations using any of these codes. This allows us to conclude that the COMSOL predictions are verified for the limiting case of spherical droplets.
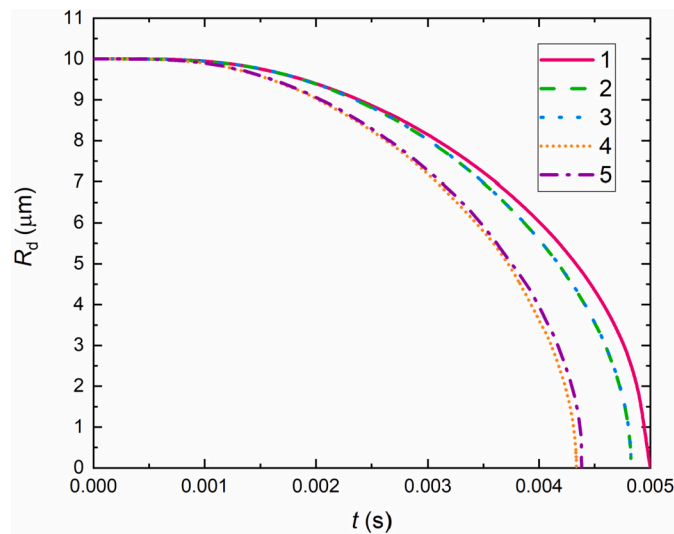
Fig. 5. Plots of effective droplet radii versus time for the same input parameters as in Section 4 predicted by the in-house MATLAB code for a spherical droplet (1), the model described in [12] for a spheroidal droplet with $\varepsilon = 1.5$ (2) and $\varepsilon = 2/3$ (3), the new model for a spheroidal droplet with $\varepsilon = 1.5$ (4) and $\varepsilon = 2/3$ (5).

5. A parametric study

As shown in the previous section, for spherical droplets the predictions of the models described in [12] and in the current paper coincide as expected. We would not expect to see such agreement between the prediction of the current model and the model in [12] for spheroidal droplets. This is because the model in [12] is based on the assumption that the temperature gradients along droplet surfaces are much smaller than those perpendicular to these surfaces. It was not possible to quantify the errors introduced by the model in [12] in the case when the gradients of this temperature along the droplet surface are small but not equal to zero. The estimation of these errors only became possible based upon direct comparison between the predictions of the model in [12] and the model described in this paper which does not make the above-mentioned assumption.

Plots of effective droplet radii versus time for the same input parameters as in Section 4 predicted by the model described in [12] for spheroidal droplets with $\varepsilon = 1.5$ and $\varepsilon = 2/3$, and the new model for the same droplets, are shown in Fig. 5. The same figure shows the plot of droplet radius versus time for a spherical droplet predicted by the MATLAB code. As can be seen from this figure, both the model described in [12] and the present model predict shorter evaporation times for spheroidal (both prolate and oblate) droplets than for spherical droplets with the same volume. At the same time, the present model predicts faster spheroidal droplet evaporation compared with that predicted by Zubkov et al. [12]. This clearly demonstrates the limitations of the model described in [12]. The latter model can be used for qualitative analysis of the effect of non-sphericity on droplet heating and evaporation but not for its quantitative analysis in the general case. Note that the curves predicted in [12] for prolate and oblate droplets almost coincide.

In what follows in this section the focus will be on the parametric study of the predictions of the new model.

Temperature profiles in prolate and oblate droplets at four time instants for the same parameters as in Fig. 5 are shown in Fig. 6. As follows from Fig. 6, the maximal temperatures at the droplet surfaces are predicted in the regions of maximal curvature (poles in prolate droplets and equators in oblate droplets). In [10] it was shown that the heat and mass fluxes on the surface of a spheroidal droplet are proportional to the fourth root of the surface Gaussian curvature. This means that, in the case of a droplet exposed to a hot environment, the region with the highest curvature is expected to reach the highest liquid temperature and vice versa. This agrees with the prediction of the model described in [12]. In both cases shown in Fig. 6 the difference between the surface and central temperatures can be clearly seen until the late stages of droplet evaporation, although this difference decreases with time.

Plots of ε, absolute values of the temperature difference at the equator and the pole, and the ratios a_z'/a_r' versus time for prolate (with initial $\varepsilon = 1.5$ and $\varepsilon = 2$) and oblate (with initial $\varepsilon = 2/3$ and $\varepsilon = 1/3$) droplets are presented in Fig. 7.

As can be seen in Fig. 7a, ε for prolate spheroidal droplets slowly decreases with time, while that for oblate spheroidal droplets slowly increases with time. This means that the shapes of both prolate and oblate droplets become more spherical. This result is consistent with the one predicted by Zubkov et al. [12], although the speeds of these processes were slower compared with the predictions of [12].

As follows from Fig. 7b, for both prolate and oblate droplets the values of ΔT initially increase with time, reach maximal values and then decrease with time until ΔT becomes close to zero at times close to 4 ms. The initial increase in temperature difference between poles and equator is due to the already mentioned differences in the heat fluxes due to the different surface curvatures. Then the internal heat transfer due to finite liquid thermal conductivity leads to a reduction in these differences. This result is also consistent with the prediction of the model in [12] except that the latter model predicted finite ΔT until the final stage of droplet evaporation at t close to 5 ms.

Fig. 7c shows that a_z'/a_r' for the prolate droplet initially increases with time, reaches the maximal value and then decreases with time. For the oblate droplet the same figure shows that a_z'/a_r' initially decreases with time, reaches the minimal value and then
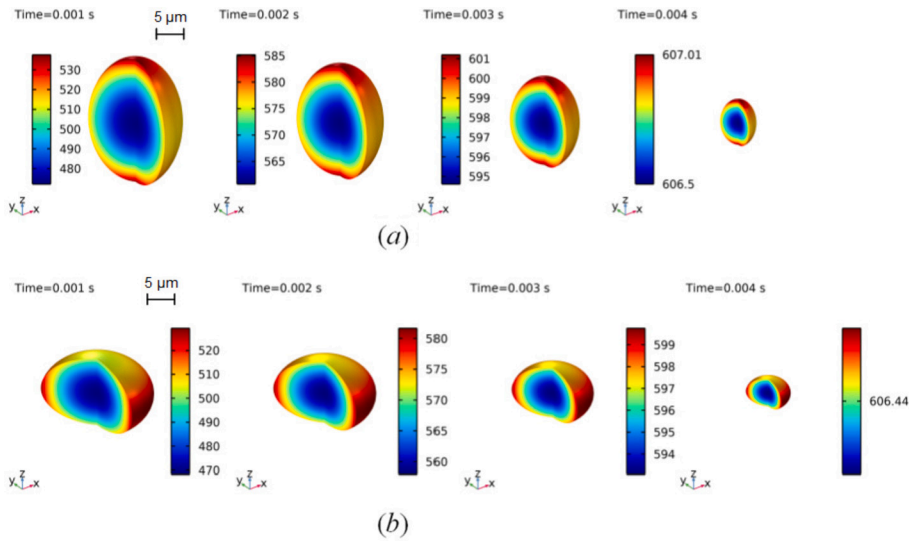
Fig. 6. Temperature profiles in a prolate ($\varepsilon = 1.5$) (a) and oblate ($\varepsilon = 2/3$) droplets at four time instants for the same parameters as in Fig. 5.

increases with time. These results are consistent with those described by Zubkov et al. [12] although the numerical values of this ratio predicted by both models at specific time instants were slightly different.

Plots of effective droplet radii versus time for prolate and oblate droplets with various ε and the same input parameters as in Figs. 5-7 are shown in Fig. 8. As follows from this figure, increasing ε for prolate droplets and a reduction in this parameter for oblate droplets lead to an increase in droplet evaporation speed. This is an expected result as in both cases the surface areas of droplets with the same volume increase and the local Gaussian curvature becomes non-uniform in both cases; these two effects lead to the intensification of droplet evaporation [10].

The results for large and small values of ε shown in this figure could not be obtained using the model described in [12] as in these cases the values of the temperature gradients along the droplet surfaces are expected to be comparable with these gradients in the direction perpendicular to the droplet surface.

Plots similar to those presented in Fig. 8 but for $\left(R_d / R_{d0}\right)^2$ versus time are shown in Fig. 9. As can be clearly seen from Fig. 9, except during the initial stage of the droplet heating and evaporation processes (heat-up period), $\left(R_d / R_{d0}\right)^2$ linearly decreases with time for both spherical and non-spherical droplets. This shows that the non-sphericity of droplets does not affect the validity of the well-known d^2-law for stationary or slowly moving droplets (for fast moving droplets this law turns into the 1.5 power law [16]). At the same time it follows from Fig. 9 that non-sphericity of droplets strongly affects the duration of the heat-up period. This period is substantially shorter for droplets with small and large aspect ratios compared with spherical droplets.

Plots of average heating rate and mass evaporation flux of droplets versus time for the same input parameters as in Fig. 9 for prolate and oblate spheroids, and for a sphere, are presented in Fig. 10. The average mass evaporation presented in Fig. 10 was calculated as

$$m_e'' = \sqrt{\left(m_{dr}''\right)^2 + \left(m_{dz}''\right)^2},$$

where subscripts r and z refer to radial and axial directions, respectively.

As can be seen from this figure, the heating rates of both prolate and oblate spheroids are larger than that for a sphere at the beginning of the process and smaller than that for a sphere at the end of the process. In all cases the mass evaporation fluxes of both prolate and oblate spheroids are larger than that for a sphere. The decrease in the heating rate with time for both spheroidal and spherical droplets is attributed to the rise in average droplet surface temperatures with time. The higher heating rate of spheroidal droplets compared with spherical ones at the initial stage of the heating process is linked with the higher than average surface temperature rise near the poles for prolate droplets and equators for oblate droplets. Then the temperatures at the poles and equators of spheroidal droplets start to level, and by about 1.2 ms the temperature gradient along the droplet surfaces reduces to less than 5 K/μm. At this time instant the heating rates of spheroidal and spherical droplets are equal. The fact that at longer times dT/dt becomes smaller for spheroidal droplets than for spherical is linked with the fact that at these times the average evaporation flux from spheroidal droplets is noticeably larger than that from spherical droplets.

6. Validation of the model

It has not been easy to perform the experimental validation of the results predicted by our new model due to the rather restrictive assumptions of the model (e.g. the assumption that the droplets retain their spheroidal shape, without oscillation). Among relatively few sets of experimental data supporting our modelling results we can mention the observation by Al Zaitone [21] that the aspect
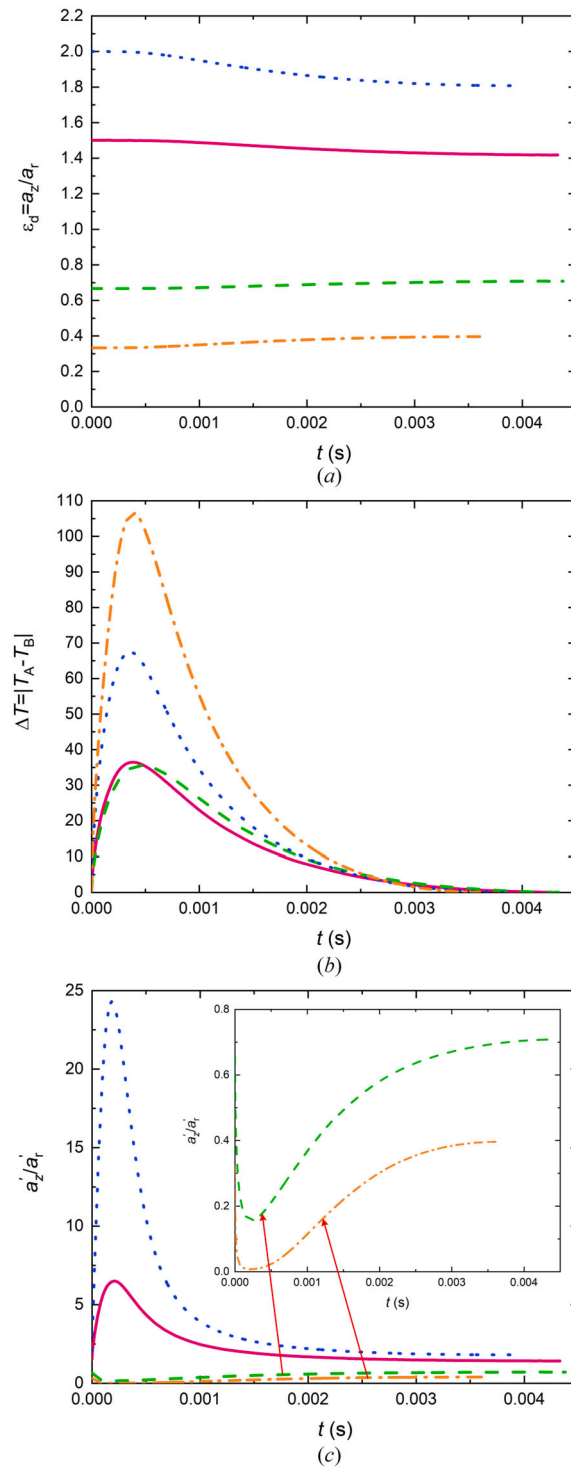
Fig. 7. Plots of $\varepsilon = a_z/a_r$ versus time (a); absolute values of the temperature difference at points A (equator) and B (pole) (see Fig. 3) (ΔT) versus time (b); ratio a_z'/a_r' (the primes show the derivatives with respect to time) versus time (c); for the same input parameters as in Figs. 5 and 6. Results for prolate (with initial $\varepsilon = 1.5$ and $\varepsilon = 2$) and oblate (with initial $\varepsilon = 2/3$ and $\varepsilon = 1/3$) droplets are shown as solid, dotted, dashed and dashed-dotted curves, respectively.
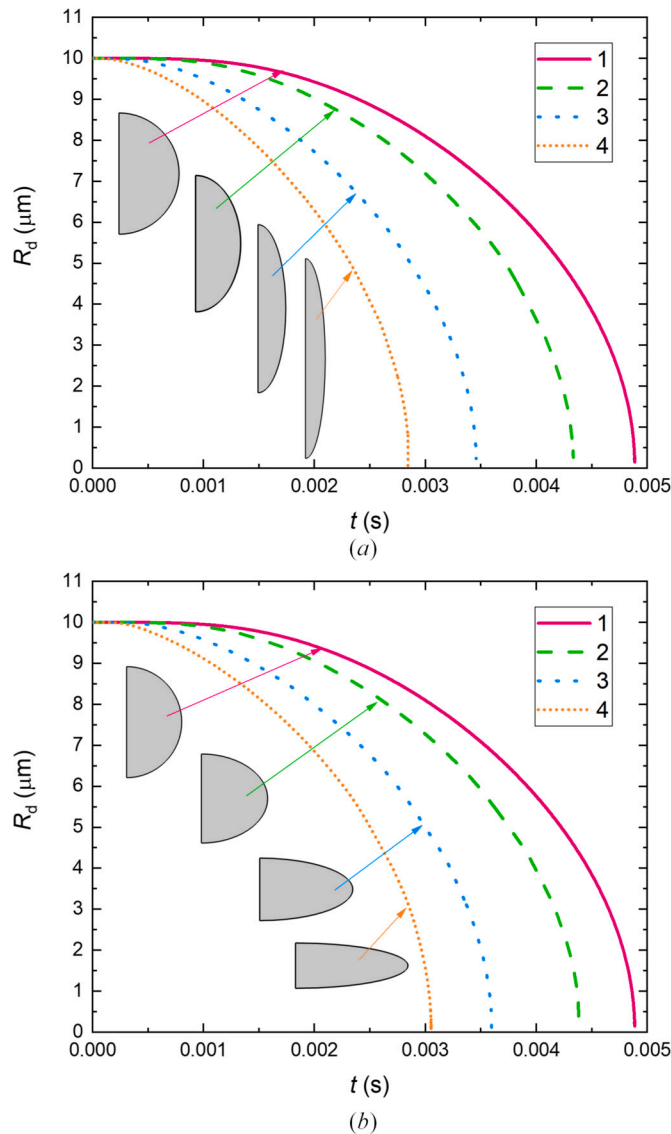
Fig. 8. Plots of effective droplet radii versus time for the same input parameters as in Figs. 5-7 except for different initial ε. (a) Prolate droplets with initial $\varepsilon = 1$ (1), $\varepsilon = 1.5$ (2), $\varepsilon = 3$ (3), $\varepsilon = 5$ (4). (b) Oblate droplets with initial $\varepsilon = 1$ (1), $\varepsilon = 2/3$ (2), $\varepsilon = 1/3$ (3), $\varepsilon = 1/5$ (4).

ratio of levitated evaporating methanol oblate droplets remains almost constant (see their Figure 5). This is consistent with the results presented in Fig. 7a. Also, Al Zaitone [21] observed that the d^2-law for stationary droplets remains valid for spheroidal droplets which is consistent with the results presented in Fig. 9.

The evaporation of steady-state oblate spheroidal droplets moving in a gas flow was observed by Pruppacher and Bear [22] and Birouk and Fabbro [23]. We are not aware of any observations of evaporation of prolate spheroidal droplets. Note that the model in its present form is not applicable to the analysis of oscillating droplets, unless the typical droplet heating and evaporation times ($t_d = \frac{R_d^2}{D_v}$ and $t_e = \frac{m_d}{\dot{m}_{ev}} = \frac{R_d^2 \rho_l}{3\rho_g D_v \ln(1+B_M)}$) are much shorter than the droplet deformation time during the oscillation process $\left(t_o = \sqrt{\frac{\rho_L R_d^3}{\sigma}} \right)$ (see [24,25] for the details).

In in-house experiments, specifically designed to validate the new model, evaporation of oblate kerosene droplets was investigated at room temperature and atmospheric pressure. A coordinate mechanism was used to introduce the droplets into the registration area, at the end of which was a nichrome wire holder of diameter 0.2 mm. A Finnpipette Novus electronic dispenser, with liquid intake from 0.5 to 12.5 µl (with steps of 0.01 µl), was used to generate the droplets. Direct intake of liquid was carried out by special interchangeable tips, which were equipped with electronic dispensers. The initial droplet volume was 5 ± 0.02 µl. The initial droplet temperature was controlled by a thermocouple and maintained at 300 ± 5 K. The experiments were performed at atmospheric pressure, assumed to be equal to 101325 Pa; gas temperature was controlled by a thermocouple and maintained at 300 ± 5 K. The registration
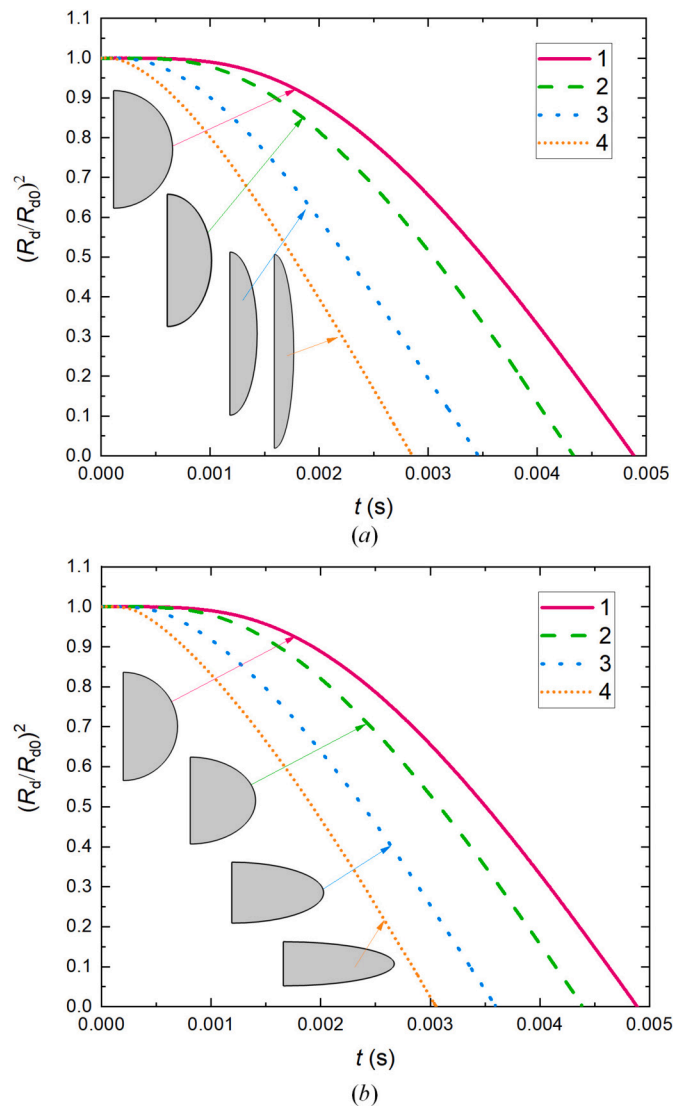
Fig. 9. The same as in Fig. 8 but for $\left(R_d/R_{d0}\right)^2$ versus time.

area was illuminated by a Qantel 'Evergreen 70' pulsed solid-state Nd:YAG laser. The droplet evaporation processes were recorded with the help of an ImperX 'IGV B2020M' cross-correlation CCD video camera. Frame resolution was 2048×2048 pixels, interframe delay was 1 s. The process of movement of the droplets from the place of their generation to the registration area took about 0.5 s at a speed of 0.2 ± 0.05 m/s.

The video frames produced during the experiments were processed using specially developed MatLab software. The latter was used to infer droplet sizes during their evaporation, from video images. Video frames showing the changes in the shapes of droplets were transferred into avi format, and then into a sequence of 8-bit black and white images. In the following step the images were binarised. The binarisation threshold was chosen individually for each series of experiments using Otsu's method. The 'fill the gaps' function was used to fill the empty areas formed due to light glare reflected from the surface of non-spherical droplets, and the holder after the subtraction procedure. At the final stage, the number of pixels of the image occupied by a non-spherical and asymmetrical droplet was determined, followed by calculation of the actual area occupied by this droplet. The equivalent radius was estimated as the radius of a circle with an area equal to the actual area occupied by the droplet. Each experiment was repeated 3 times. The systematic errors of measured droplet initial radii did not exceed 0.0035 mm. Random errors Δr were estimated as $\Delta r = t(a_c, n)S$, where S is the root squared deviation, and $t(a_c, n)$ is the Student's coefficient. The latter depended on the number of measurements n and confidence level a_c, taken equal to 0.95. Total errors (random and systematic) of the measurements did not exceed ± 0.05 mm.

The observed normalised droplet radii squared $((R_d/R_{d0})^2)$ and the ones predicted by the model for an oblate kerosene droplet are compared in Fig. 11. Kerosene was approximated by n-decane. The properties of the n-decane were taken from [26]. Two values of ε were considered in the modelling: $\varepsilon = 1$ (droplet deformation was ignored) and $\varepsilon = 0.9$ (actual value of ε for the droplets used in
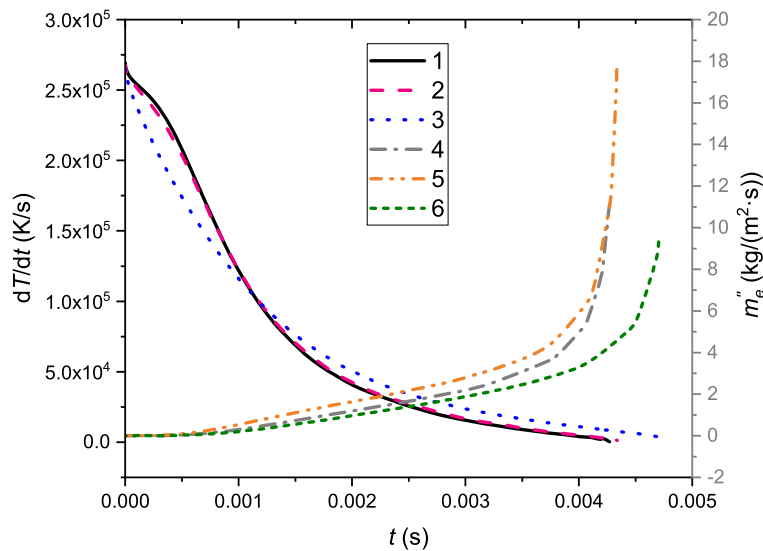
Fig. 10. Plots of average heating rate (dT/dt) of prolate ($\varepsilon = 1.5$) (1) and oblate ($\varepsilon = 2/3$) (2) spheroids, and for a sphere ($\varepsilon = 1$) (3); mass evaporation flux (m_e'') of prolate ($\varepsilon = 1.5$) (4) and oblate ($\varepsilon = 2/3$) (5) spheroids, and for a sphere ($\varepsilon = 1$) (6) versus time for the same parameters as in Fig. 9.
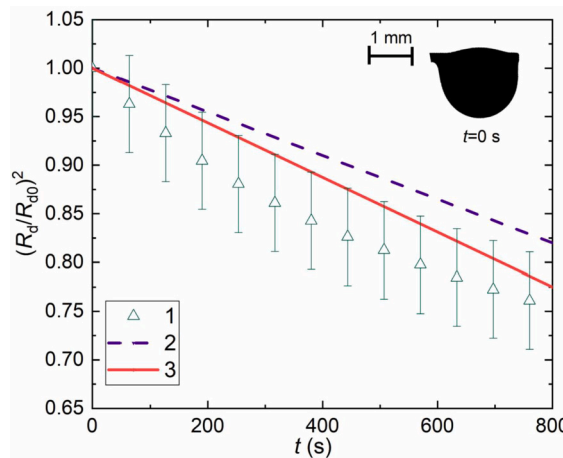

Fig. 11. Comparison of the results of numerical simulation and experimental data for oblate kerosene droplets with $\varepsilon = 0.9$: (1) – experimental data; (2) – model prediction using the assumption that $\varepsilon = 1$; (3) – model prediction considering the actual value of $\varepsilon = 0.9$.

the experiments). As can be seen from Fig. 11, the prediction of the model with $\varepsilon = 0.9$ is much closer to experimental results than the prediction of the model with $\varepsilon = 1$. The agreement between the model prediction and experimental data when $\varepsilon = 0.9$ can be considered satisfactory for the conditions of the experiment in which the droplet shapes are rather crudely approximated by those of spheroids.

7. Conclusions

A new mathematical model for spheroidal droplet heating and evaporation is developed. The new model considers the effect of liquid finite thermal conductivity and is applicable to a wide range of aspect ratios (eccentricities), provided that Correlation (31) is valid. The model is based on the previously obtained analytical solution for the vapour mass fraction at the droplet surface (Expression (4)) and Correlation (31) for the convective heat transfer coefficient incorporated into the numerical code. The heat transfer equation in the liquid phase is solved numerically using the finite-element heat transfer module of COMSOL Multiphysics.

In the limiting case of spherical droplets the predictions of the new model are shown to coincide with the predictions of the MATLAB code specifically developed for spherical droplets and the predictions of the code for spheroidal droplets (close to spherical droplets), developed by Zubkov et al. [12] in the limiting case of spherical droplets.

It is shown that the lifetimes of spheroidal (prolate and oblate) droplets are shorter than those of spherical droplets of the same volume, in agreement with the results presented in [12]. The difference in the lifetimes of spheroidal and spherical droplets, predicted

Table 1
Approximation of transport and thermodynamic properties of fluids.

Parameter	Approximation	Unit
p_{sat}^*	$\exp\left[8.1948 - 7.8099\left(300/T_s\right)\right.$ $\left. -9.0098\left(300/T_s\right)^2\right]$	bar
T_{ref}	$(2T_s + T_\infty)/3$	K
Y_{ref}	$(2Y_s + Y_\infty)/3$	–
k_l	$0.1405 - 0.00022(T - 300)$	W/(m·K)
c_l	$2.18 + 0.0041(T - 300)$	kJ/(kg·K)
k_g	$0.0036 + 0.0252\left(\frac{T_{ref}}{300}\right) - 0.00189\left(\frac{T_{ref}}{300}\right)^2$	W/(m·K)
c_{pv}	$0.2979 + 1.4394\left(\frac{T_{ref}}{300}\right) + 0.1351\left(\frac{T_{ref}}{300}\right)^2$	kJ/(kg·K)
ρ_g	$\left(M_v p_{sat} + M_a \cdot (p_g - p_{sat})\right)/\left(R_u T_{ref}\right)$	kg/m³
L_l	$37440 \cdot \left(T_{cr} - T_{ref}\right)^{0.38}$	J/kg

by the new model, however, is shown to be larger than that predicted by Zubkov et al. [12]. This difference is shown to increase with increasing aspect ratios for prolate droplets and decreasing aspect ratios for oblate droplets.

As in the case of stationary spherical droplets, the d^2-law is shown to be valid for spheroidal droplets (both prolate and oblate) after the completion of the heat-up period. This prediction of the model is shown to be consistent with experimental observations. The duration of the heat-up period is shown to decrease with increasing aspect ratios for prolate droplets and decreasing aspect ratios for oblate droplets.

The maximal surface temperatures are predicted near the regions where the surface curvature is maximal. The absolute values of the difference between the droplet temperatures at the poles and equator are shown to increase initially. This is followed by a decrease leading to homogeneous surface temperature at the final stage of droplet evaporation.

The aspect ratios are shown to be weak functions of time, in agreement with experimental observations.

The model validation was performed based on in-house experimental data for the evaporation of oblate kerosene droplets.

Declaration of competing interest

Data availability

Data will be made available on request.

Acknowledgements

Appendix A. Approximation of transport and thermodynamic properties of n-dodecane and air

Approximations of key thermodynamic and transport properties of air and of liquid and vapour n-dodecane are presented in Table 1. Note that the expression for p_{sat} given in this table is valid at $T \leq 0.99T_{cr}$. At higher temperatures it is approximated as [12]:

$$p_{sat} \exp\left[\frac{15(T_s - 0.99T_{cr})}{0.99T_{cr}}\right].$$

Since the effects of thermal swelling were not considered, the temperature dependence of liquid n-dodecane density was ignored.

References

[1] E. Michaelides, Particles, Bubbles and Drops, World Scientific, New Jersey, 2006.

[2] C. Crua, M. Heikal, M. Gold, Microscopic imaging of the initial stage of diesel spray formation, Fuel 157 (2015) 140, https://doi.org/10.1016/j.fuel.2015.04.041.

[3] C. Crua, J. Manin, L. Pickett, On the transcritical mixing of fuels at diesel engine conditions, Fuel 208 (2017) 535, https://doi.org/10.1016/j.fuel.2017.06.091.

[4] R. Shah, T. Li, The thermal and laminar boundary layer flow over prolate and oblate spheroids, Int. J. Heat Mass Transf. 121 (2018) 607, https://doi.org/10.1016/j.ijheatmasstransfer.2017.12.130.

[5] N. Talebanfard, H. Nemati, B. Boersma, Heat transfer in deforming droplets with a direct solver for a coupled levelset and volume of fluid method, Int. Commun. Heat Mass Transf. 108 (2019) 104272, https://doi.org/10.1016/j.icheatmasstransfer.2019.104272.

[6] S.S. Sazhin, Droplets and Sprays: Simple Models of Complex Processes, Mathematical Engineering, Springer, 2022.

[7] C. Niven, On the conduction of heat in ellipsoids of revolution, Philos. Trans. R. Soc. Lond. 171 (1880) 117, https://doi.org/10.1098/rstl.1880.000.

[8] S. Kang, E. Dehdashti, H. Masoud, Conduction heat transfer from oblate spheroids and bispheres, Int. J. Heat Mass Transf. 139 (2019) 115, https://doi.org/10.1016/j.ijheatmasstransfer.2019.04.138.

[9] D. Grow, Mass and heat transfer to an ellipsoidal particle, Combust. Flame 80 (1990) 209, https://doi.org/10.1016/0010-2180(90)90128-E.

[10] S. Tonini, G.E. Cossali, An exact solution of the mass transport equations for spheroidal evaporating drops, Int. J. Heat Mass Transf. 60 (2013) 236, https://doi.org/10.1016/j.ijheatmasstransfer.2013.01.001.

[11] J. Li, J. Zhang, A theoretical study of the spheroidal droplet evaporation in forced convection, Phys. Lett. A 378 (2014) 3537, https://doi.org/10.1016/j.physleta.2014.10.020.

[12] V. Zubkov, S. Tonini, G.E. Cossali, C. Crua, M. Heikal, S.S. Sazhin, Mathematical modelling of heating and evaporation of a spheroidal droplet, Int. J. Heat Mass Transf. 108 (2017) 2181, https://doi.org/10.1016/j.ijheatmasstransfer.2016.12.074.

[13] S. Tonini, G.E. Cossali, Modelling of heat and mass transfer from spheroidal drops with non-uniform surface temperature, Int. J. Heat Mass Transf. 121 (2018) 747, https://doi.org/10.1016/j.ijheatmasstransfer.2018.01.040.

[14] G.E. Cossali, S. Tonini, Drop Heating and Evaporation: Analytical Solutions in Curvilinear Coordinate Systems, Mathematical Engineering, Springer, 2021.

[15] J.G. Wissink, H. Herlina, Surface-temperature-induced Marangoni effects on developing buoyancy-driven flow, J. Fluid Mech. 962 (2023) A23, https://doi.org/10.1017/jfm.2023.263.

[16] E. Starinskaya, N. Miskiv, A. Nazarov, V. Terekhov, V. Terekhov, O. Rybdylova, S.S. Sazhin, Evaporation of water/ethanol droplets in an air flow: experimental study and modelling, Int. J. Heat Mass Transf. 177 (2021) 121502, https://doi.org/10.1016/j.ijheatmasstransfer.2021.121502.

[17] Z. Pan, S. Dash, J.A. Weibel, S. Garimella, Assessment of water droplet evaporation mechanisms on hydrophobic and superhydrophobic substrates, Langmuir 29 (51) (2013) 15831–15841, https://doi.org/10.1021/la4045286.

[18] Z. Pan, J.A. Weibel, S. Garimella, Influence of surface wettability on transport mechanisms governing water droplet evaporation, Langmuir 30 (32) (2014) 9726–9730, https://doi.org/10.1021/la501931x.

[19] Z. Pan, J.A. Weibel, S. Garimella, Transport mechanisms during water droplet evaporation on heated substrates of different wettability, Int. J. Heat Mass Transf. 152 (2020) 119524, https://doi.org/10.1016/j.ijheatmasstransfer.2020.119524.

[20] H. Fugmann, L. Schnabel, B. Frohnapfel, Heat transfer and pressure drop correlations for laminar flow in an in-line and staggered array of circular cylinders, Numer. Heat Transf., Part A, Appl. 75 (1) (2019) 1–20, https://doi.org/10.1080/10407782.2018.1562741.

[21] B. Al Zaitone, Oblate spheroidal droplet evaporation in an acoustic levitator, Int. J. Heat Mass Transf. 126 (2018) 164, https://doi.org/10.1016/j.ijheatmasstransfer.2018.06.029.

[22] J. Pruppacher, K. Bear, A wind tunnel investigation of the internal circulation and shape of water drops falling at terminal velocity in air, Q. J. R. Meteorol. Soc. 96 (1970) 247, https://doi.org/10.1002/qj.49709640807.

[23] M. Birouk, S. Fabbro, Droplet evaporation in a turbulent atmosphere at elevated pressure – experimental data, Proc. Combust. Inst. 34 (2013) 1577, https://doi.org/10.1016/j.proci.2012.05.092.

[24] S. Tonini, G.E. Cossali, An evaporation model for oscillating spheroidal drops, Int. Commun. Heat Mass Transf. 51 (2014) 18, https://doi.org/10.1016/j.icheatmasstransfer.2013.12.001.

[25] S. Tonini, G. Varma RajaKochanattu, G.E. Cossali, The effect of evaporation on the oscillation frequency of an inviscid liquid drop, Int. Commun. Heat Mass Transf. 116 (2020) 104609, https://doi.org/10.1016/j.icheatmasstransfer.2020.104609.

[26] C.L. Yaws, Yaws' Handbook of Thermodynamic and Physical Properties of Chemical Compounds, Knovel, 2003.